Author for correspondence:
Federico Covi, E-mail: fcovi@alaska.edu

cambridge.org/jog

Challenges in modeling the energy balance and melt in the percolation zone of the Greenland ice sheet

Federico Covi[1] ![ORCID], Regine Hock[1,2] ![ORCID] and Carleen H. Reijmer[3] ![ORCID]

[1]Geophysical Institute, University of Alaska Fairbanks, Fairbanks, AK, USA; [2]Department of Geoscience, University of Oslo, Oslo, Norway and [3]Institute for Marine and Atmospheric Research, Utrecht University, Utrecht, The Netherlands

Abstract

Increased surface melt in the percolation zone of the Greenland ice sheet causes significant changes in the firn structure, directly affecting the amount and timing of meltwater runoff. Here we force an energy-balance model with automatic weather stations data at two sites in the percolation zone of southwest Greenland (2040 and 2360 m a.s.l.) between spring 2017 and fall 2019. Extensive model validation and sensitivity analysis reveal that the skin layer formulation used to compute the surface temperature by closing the energy balance leads to a consistent over-estimation of melt by more than a factor of two or three depending on the site. In contrast, model results match the observations well when the model is forced by observed surface temperatures; however, unexplained residuals in the energy balance occur. The sensible and ground heat flux differ markedly in the two simulations accounting largely for the difference in modeled melt amounts. This indicates that the energy available for melt is highly sensitive to small changes in surface temperature. Thus, regional climate models that also use the skin layer formulation may have a bias in surface temperature and melt energy in the percolation zone of the ice sheet.

1. Introduction

The Greenland ice sheet is the second largest body of ice on Earth and it has the potential to contribute 7.4 m to sea level rise if melted entirely (Intergovernmental Panel on Climate Change, 2014; Morlighem and others, 2017). Over the last three decades, its ice mass loss rate doubled, increasing from 119 Gt a^{-1} over the period 1992–2011, to 244 Gt a^{-1} over the period 2012–17 (Shepherd and others, 2020), making it responsible for $\sim$15% of the observed contemporary sea level rise (Cazenave and others, 2018). Of the total ice sheet mass loss, more than 50% can be attributed to surface mass balance (55 $\pm$ 5% between 1998 and 2018, Mouginot and others (2018); 68% between 2009 and 2012, Enderlin and others (2014)), which is becoming increasingly more negative (Mote, 2007). Melt events and melt areal extent have expanded to higher elevations (Tedesco, 2007; Fettweis and others, 2011), reaching areas of the percolation and dry snow zone that previously experienced only little to no melt. This led to significant changes in the firn structure, such as the formation of thick impermeable ice layers in the lower percolation zone (Machguth and others, 2016). These ice layers have impeded meltwater percolation, causing meltwater to directly runoff and increasing the total ice sheet runoff area by 26% since 2001 (MacFerrin and others, 2019).

In order to better quantify and understand the ice sheet's contribution to sea level rise, it is thus fundamental to better constrain surface melt, which ultimately controls the surface mass balance and changes in the firn structure. Regional climate models (RCMs) such as the Modele Atmospherique Regionale (MAR) (Fettweis and others, 2017), the HIRHAM RCM (Christensen and others, 2006) and the Regional Atmospheric Climate Model (RACMO2) (Noël and others, 2018) are typically used to model the surface mass balance over the entire ice sheet. These are forced by either global atmospheric reanalysis data or general circulation models, allowing for projections as well as simulations of the past. Because RCMs are computationally very demanding, they are typically run on grids with resolutions on the order of $\sim$10 km, although higher resolutions (Noël and others, 2019) and downscaled results (Noël and others, 2016) are now becoming available.

However, small-scale local studies are needed to evaluate these large-scale models and investigate the physical processes in more detail. These studies typically use 1-D models of varying complexity, forced by in situ meteorological observations from automatic weather stations (AWSs), to quantify the surface energy balance and the resulting melt. These models have become more complex since their first applications in Greenland in the 1980s (Braithwaite and Olesen, 1990; Greuell and Konzelmann, 1994), and nowadays typically include modules that simulate subsurface processes such as firn temperature, meltwater percolation and refreezing and firn densification (Charalampidis and others, 2015; Vandecrux and others, 2018, 2020; Samimi and others, 2021). Studies focused on different aspects such as energy-balance partitioning (Braithwaite and Olesen, 1990; Greuell and Konzelmann, 1994; Henneken and others, 1994; Van Den Broeke, 2008), seasonal and interannual variability (Van Den Broeke and others, 2011), surface meltwater discharge modeling (Van As and
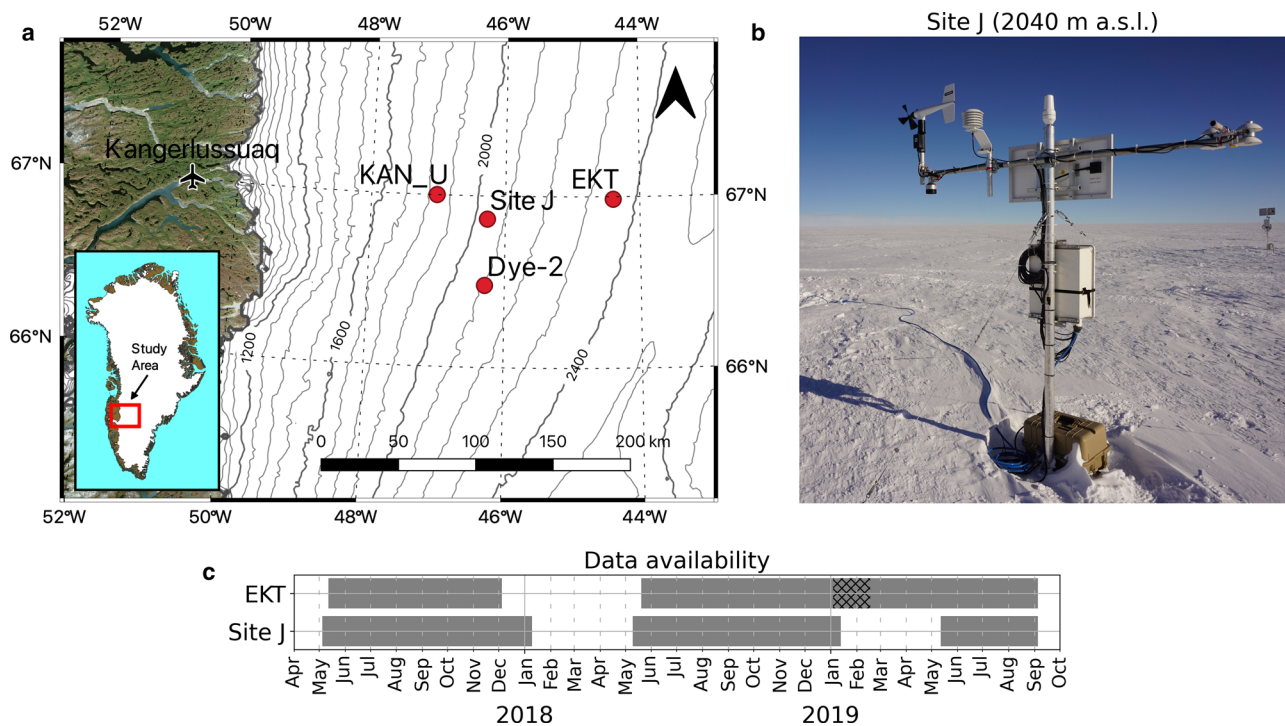
Fig. 1. (a) Study area and locations of sites relevant for this study; elevation contours in m a.s.l. are based on the ArcticDEM 1 km v.3.0 product by Polar Geospatial Center (Porter and others, 2018) adjusted with the EGM2008 geoid offset (Pavlis and others, 2012). (b) The AWS at Site J in Spring 2017. (c) Weather stations data coverage at EKT and Site J; the hatched area between 4 January and 17 February 2019 at EKT shows a period during which the sonic ranger (SR50) was malfunctioning; data gaps are due to power failure; ticks refer to the first day of each month.

others, 2012) and long-term changes in surface energy fluxes (Kuipers Munneke and others, 2018; Huai and others, 2020). Most of the previous local surface energy-balance studies have been carried out at sites along the K-transect, a historical transect in the ablation zone east of Kangerlussuaq in southwest Greenland (Fig. 1), where the surface mass balance has been measured since 1990 and several AWSs have recorded atmospheric conditions and radiative fluxes since 1993 (Smeets and others, 2018).

In contrast, energy-balance studies in the percolation zone are fewer and more recent. Charalampidis and others (2015) modeled the surface energy balance at the KAN_U site (1840 m a.s.l., the highest site of the K-transect) during the period between 2009 and 2013, showing evidence of enhanced melt and reduction of the refreezing capacity of firn. Vandecrux and others (2018) and Vandecrux and others (2017) applied a multilayer firn model to study changes in the firn properties such as density and cold content at different sites in the percolation and dry snow zone of the Greenland ice sheet. Samimi and others (2021) combined modeling efforts with time-domain reflectometry measurements to monitor and constrain meltwater and refreezing processes at the Dye-2 site (2120 m a.s.l., southeast of KAN_U). However, none of these studies focused on assessing the model's ability to reproduce melt accurately. To our knowledge, a point energy-balance model, including radiation penetration and deep water percolation, has not been evaluated in detail in the percolation zone of the Greenland ice sheet.

In this study, we use data from two weather stations in the percolation zone in southwest Greenland to force a surface energy-balance model coupled to a multilayer subsurface model. We evaluate model results against independent observations of surface height, and surface and subsurface temperatures. We perform extensive experiments to assess model sensitivity to input forcings, model parameters and parameterizations. Furthermore, we account for the penetration of shortwave radiation into the snow, following the approach of Kuipers Munneke and others

(2009, 2012), and deep water percolation, following the approach of Marchenko and others (2017), and we assess their impact on the surface energy balance and melt estimates.

2. Study area and observations

Two AWSs were installed during spring 2017 at Site J (2040 m a.s.l.) on 28 April and at EKT (2360 m a.s.l.) on 6 May (Fig. 1a) and operated until 5 September 2019. The sites are located in the southwest percolation zone of the Greenland ice sheet in proximity to the K-transect, ~80 km apart from each other and more than 150 km from the ice margin. Both sites have been subject to previous studies, including a >200 m firn core drilled at Site J in 1989 (Kameda and others, 1995) and shallow firn core collection between 2013 and 2017 at EKT (Machguth and others, 2016; MacFerrin, 2018).

The stations recorded near-surface air temperature, relative humidity, wind speed and direction, shortwave incoming and reflected radiation, longwave incoming and outgoing radiation and relative surface height (Fig. 1b, Table I). Subsurface

Table 1. AWSs' instruments and accuracy

Variable	Instrument	Accuracy
Air temperature	Vaisala HMP60	0.6°C
Relative humidity	Vaisala HMP60	5% < 90%, 7% > 90%
Wind speed	RM Young 05103	0.3 m s^{-1}
Wind direction	RM Young 05103	3°
Shortwave radiation	Hukseflux NR01	20% for hourly sums
Longwave radiation	Hukseflux NR01	20% for hourly sums
Tiltmeter	Turck B2N45H	0.1°
Surface height	Campbell SR50A	0.01 m
Firn temperature	Geokon 3810-2	0.2°C
	Omega 44031[a]	0.1°C
	PS302J2[b]	0.1°C

Additional firn temperature thermistors were deployed in May 2019 at Site J[a] and EKT[b].

temperatures were measured at 28 depths, with the first 23 thermistors spaced 0.5 m apart, and the next five thermistors spaced 1.0 m apart. The uppermost sensor was at a depth of 1 m below the snow surface at both sites during installation in spring 2017. Two additional thermistors (Table I) were added in May 2019 at a depth of 0.45 and 0.70 m at Site J and 0.78 and 1.15 m at EKT. Meteorological variables were sampled every 5 min, while surface height and subsurface temperatures were sampled every hour. At Site J, the instruments were mounted to a 5 m long mast drilled initially 3 m into the firn and secured with three guy wires (Fig. 1b). At EKT, instruments were mounted to an already existing station (MacFerrin and others, 2022). At both sites, instruments were installed 2 m above the surface in May 2017 and reset to 2 m in May 2018 to avoid instruments' burial due to net accumulation. The instruments' height above the surface varies between 1.25 and 2.18 m at Site J and 1.39 and 2.10 m at EKT. Due to power failure, the stations failed to record data during part of the winter; data availability is shown in Fig. 1c.

The two data series have been quality-checked and corrected when necessary. The summer (June, Julyand August) mean air temperature (T_{air}) was below freezing at both sites for all 3 years on record, ranging between -6.2 and $-4.4°$C at Site J and -9.0 and $-6.9°$C at EKT, with 2017 and 2019 being the coldest and warmest summers, respectively. Maximum air temperatures of 7.6°C at Site J and 6.1°C at EKT were measured during summer 2019. Both relative humidity (RH) and wind speed (u) exhibit little interannual and spatial variability, with RH values between 84 and 86% at Site J and 82 and 86% at EKT and u values between 4.6 and 5.4 m s^{-1} at Site J and 3.9 and 5.0 m s^{-1} at EKT. Firn temperature ranges between -18.7 and $0.0°$C at Site J and between -23.8 and $-2.4°$ C at EKT, with the maximum values recorded during summer 2019. The average temperature ($\pm$SD) computed at depths >10 m below the surface over the entire study period is -13.4 ± 0.3 and $-19.3 \pm 0.1°$C at Site J and EKT, respectively. In close proximity to each station, an ablation stake was installed to allow independent measurements of relative surface height, useful to compare and validate the data from the sonic ranger. The relative surface height change over the whole study period (spring 2017–fall 2019) was $+1.05$ m at Site J and $+1.55$ m at EKT.

The subsurface model used in this study was initialized with firn data from two 25 m firn cores that were drilled at Site J and EKT in spring 2017 using a mechanical ice-coring drill. A detailed description of the firn cores is given in Rennermalm and others (2012). Density data from close by snow pits were used for the winter snow layer, which ranged from 0.87 m at Site J to 0.90 m at EKT in 2017.

3. Melt modeling

Here, we develop a 1-D surface energy-balance model that computes all relevant surface energy fluxes and resulting melt with hourly resolution. The model is largely based on the Distributed Energy BAlance Model (DEBAM) (Hock and Holmgren, 2005), which includes a multi-layer subsurface model that computes subsurface temperature, density and water content (Reijmer and Hock, 2008). A brief description of our model is given below. For further details we refer to Hock and Holmgren (2005) and Reijmer and Hock (2008).

3.1. Surface energy-balance model

The surface energy balance is calculated by:

$$S_{in} + S_{ref} + L_{in} + L_{out} + H + LE + Q_R + Q_G + Q_M = 0, \quad (1)$$

where S_{in} and S_{ref} are the incoming and reflected shortwave radiation, respectively, L_{in} and L_{out} are the incoming and outgoing longwave radiation, respectively, H is the sensible heat flux, LE is the latent heat flux, Q_R is the energy supplied by rain, Q_G is the energy flux into the subsurface (also referred to as ground heat flux) and Q_M is the energy available for melt. Fluxes toward the surface are defined as positive. The model uses a skin layer formulation to close the energy balance at the surface. In this approach the surface is assumed to be an infinitesimal skin layer without heat capacity that reacts instantaneously to a change in energy input. Several fluxes in Eqn (1) directly depend on the surface temperature T_s (L_{out}, H, LE, Q_G and Q_R). A bisection method is iteratively applied to find the T_s that satisfy Eqn (1) assuming $Q_M = 0$. If a positive surface temperature is found (indicating surface melt, i.e. $Q_M \neq 0$), T_s is reset to zero, and the energy balance is recalculated. The resulting non-zero Q_M is converted into melt.

The radiative fluxes S_{in}, S_{ref} and L_{in} are taken from observations at the weather stations. L_{out} is calculated from the modeled surface temperature using the Stefan–Boltzmann law, assuming an emissivity of 1. Measured L_{out} is used for model validation.

The turbulent fluxes are calculated using the bulk aerodynamic method, relating H and LE to wind speed and gradients of temperature and vapor pressure between the surface and the air (Hock and Holmgren, 2005). Wind speed and air temperature are based on observations, and vapor pressure is calculated from measurements of relative humidity. For these calculations, we assume a constant measurement height above the surface of 2 m. The effect of atmospheric stability is taken into account using the Monin–Obukhov similarity theory. Stability functions for stable atmospheric stratification are computed following Beljaars and Holtslag (1991), while stability functions for unstable atmospheric stratification are computed following Panofsky and Dutton (1984). Surface roughness length for momentum is set at a constant value of 10^{-4} m, which is found to be a good assumption at these elevations on the ice sheet (Smeets and Broeke, 2008a; Charalampidis and others, 2015). Surface roughnesses lengths for heat and moisture are calculated using the surface renewal theory (Andreas, 1987; Munro, 1990).

The energy supplied by rain Q_R is determined by the rainfall rate and the temperature difference between the air and the surface (Hock and Holmgren, 2005). The ground heat flux Q_G is calculated from the temperature gradient between the surface and the first subsurface layer using Fourier's law and the thermal conductivity provided by the subsurface model. In this calculation, modeled surface temperature from the current time step and subsurface temperature from the previous time step are used.

3.2. Subsurface model

The subsurface model is based on the SOMARS model developed by Greuell and Konzelmann (1994) and further refined by Reijmer and Hock (2008). The model calculates firn temperature, density of the dry part of the firn and liquid water content on a vertical grid, including the effect of meltwater percolation, refreezing and dry firn densification. Here the grid extends from the surface to a depth of 25 m with a total of $\sim$140 layers with varying resolution: 0.05 m from the surface to 1 m depth, 0.1 m between 1 and 10 m depth and 0.5 m below 10 m depth.

First, the temporal evolution of the firn temperature is calculated using a forward time centered space finite difference method to solve the 1-D heat equation. Boundary conditions are given by the surface temperature at the snow surface, computed by the surface energy balance model, and by a constant temperature at the bottom of the firn column, determined by observations ($-13.4°$C at Site J and $-19.3°$C at EKT). The thermal conductivity (κ) is

described as a function of the firn density, following the approach presented in Douville and others (1995).

Next, if energy is available for melting ($Q_M > 0$), the amount of melt at the surface is calculated. Meltwater and rainwater are then added to the liquid water content of the first subsurface layer. Refreezing, percolation and densification are sequentially calculated for every layer. The amount of refreezing is limited by either layer temperature, liquid water content or available pore space. If any water is still present in the layer, a small amount of it is retained in the layer against gravity due to capillary forces (irreducible water content) while the rest is allowed to percolate to the next layer. The irreducible water content is described as a function of the firn density, according to Schneider and Jansson (2004). Finally, the densification of the dry firn is calculated depending on the temperature gradient and the density following the Herron and Langway (1980) parameterization adapted by Li and Zwally (2004).

Solid precipitation is added to the first layer using observations of fresh snowfall thickness and density. The thickness for each time step was derived from total daily surface height changes in order to filter the often noisy sonic ranger data; daily values were then distributed equally over the day for the simulations. A fresh snowfall density of 350 kg m^{-3} was derived from snow pit observations at Site J and EKT in Spring 2017. This value reflects the rapid, wind-driven, compaction following snowfall events and it is in line with previous studies suggesting values between 315 and 400 kg m^{-3} for this area of the ice sheet (Charalampidis and others, 2015; Fausto and others, 2018; Vandecrux and others, 2018). The model does not account for the lateral flow of water. Subsurface layers are allowed to merge or split to maintain the initial grid configuration if they become thinner than 50% or thicker than 150% of their original thickness. This is often the case for the first layer, where thinning and thickening occur during melting and snowfalls.

3.3. Model application

The model was run at Site J and EKT from 6 May 2017 to 4 September 2019 for all the periods when meteorological data

were available (Fig. 1c). Hourly data of air temperature, relative humidity, wind speed, shortwave incoming and reflected radiation, longwave incoming radiation and solid precipitation provided the meteorological input to run the model. All the forcing inputs were taken directly from weather station observations. The model was run at 4 min resolution to assure the stability of the subsurface solver; hourly input data were linearly interpolated to match the required time step. The subsurface model was initialized with firn temperature and density data from the firn thermistor string and firn cores, respectively. When firn core data were unavailable (May 2018 at Site J and EKT, May 2019 at Site J), the firn density profile was initialized using model output from the end of that site's previous simulation adjusted to account for the correct seasonal snow depth.

3.4. Model validation

Simulations are validated against independent observations of relative surface height from both the weather station sonic ranger and ablation stakes readings (Fig. 2), surface temperature estimated from the measurements of outgoing longwave radiation using the Stefan–Boltzmann law with an emissivity of 1 (Fig. 2), and subsurface temperatures from thermistor strings (Fig. 3).

Independent in situ ablation stake readings, which provide relative surface height changes between annual field visits, match the continuous sonic ranger (SR50) data very well (Figs 2a, c). This provides confidence that the weather stations, where the sonic rangers were mounted, were not subject to sinking during the study period. In contrast, simulated relative surface heights do not agree well with these observations. Modeled surface lowering, almost entirely caused by melt, is consistently overestimated at both sites and during all three years except for EKT in summer 2017, where only little melt occurred. Maximum differences between observed and simulated relative surface height up to 0.47 m at Site J and 0.42 m at EKT are recorded during summer 2019 when surface melting was most pronounced.

The comparison of modeled hourly surface temperatures with those derived from the measurements of outgoing longwave
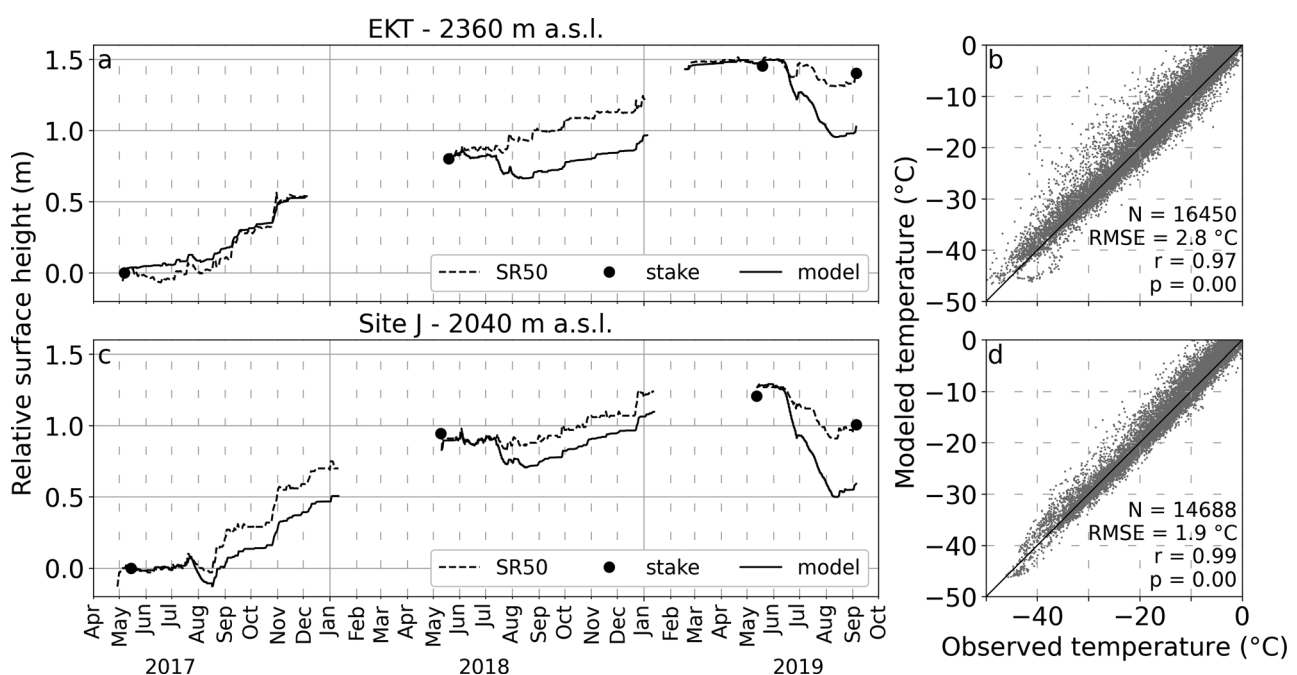

Fig. 2. Model validation at EKT (a, b) and Site J (c, d). (a, c) Modeled hourly relative surface height compared to measurements from the AWS sonic ranger (SR50) and ablation stake between May 2017 and September 2019. (b, d) Modeled vs observed hourly surface temperature, with the 1:1 line in black. N is the number of samples, RMSE the root mean square error, r the correlation coefficient and p the p-value.
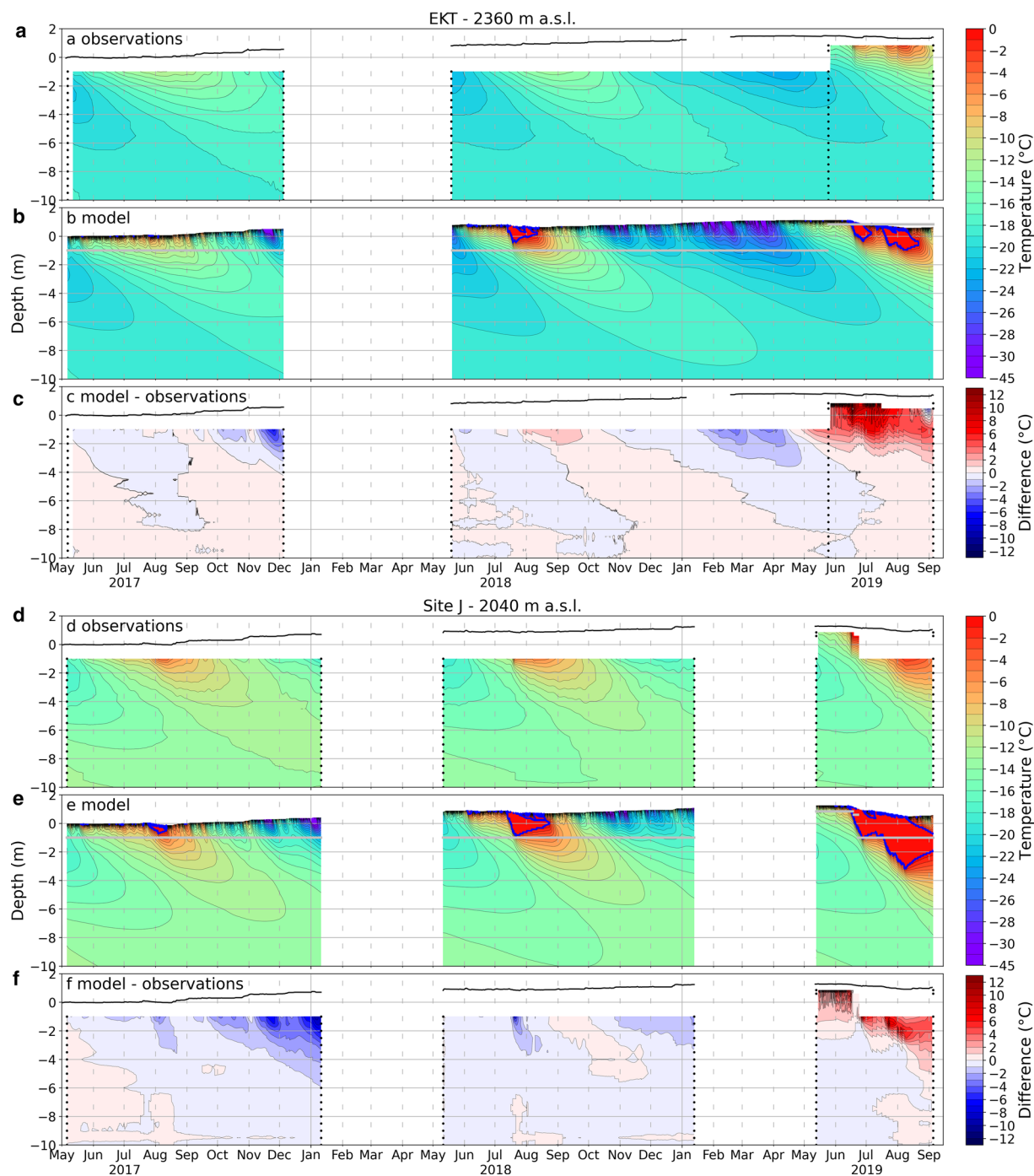
Fig. 3. Hourly (a, d) measured, (b, e) modeled subsurface temperatures and (c, f) their differences for the uppermost 10 m between May 2017 and September 2019 at EKT (a–c) and Site J (d–f). The depths are relative to the snow surface on the date of installation in early May 2017. Black lines and black dots in (a, c, d, f) indicate the observed relative surface height and the thermistors position, respectively. Blue lines in (b, e) contour the boundary of subsurface liquid water. Gray lines in (b, e) indicate the depth of the uppermost thermistor. Data from the new thermistors installed in May 2019 are omitted in (a, c, d, f) when the sensors reached the surface or were affected by solar radiation penetration.

radiation reveals that the model tends to overestimate T_s, especially during the summer months when melt occurs at the surface (Figs 2b, d). The average difference between modeled and observed temperatures is +1.11°C at EKT and +0.59°C at Site J over the whole study period, increasing to +1.93° and +1.31°C, respectively when only the summer months (June, July and August) are considered. The correlation coefficient between hourly model results and observations is 0.97 and 0.99, and root mean square error is 2.8° and 1.9°C at EKT and Site J, respectively.

Figure 3 shows simulated and observed subsurface temperatures and their differences. Temperatures below −10 m depth (not shown) remain constant at both sites and model results

agree well with the observations. Simulated temperatures generally match the observations at depths below 4 m well, but the model tends to underestimate near-surface (between 0 and 4 m depths) temperatures during the winter and overestimate them during the summer (Figs 3c, f). The overestimation of summer temperatures is more evident in 2019 when melt was more pronounced. Furthermore, in May 2019, two new thermistors were installed at both sites in that year's winter snow (~first meter), allowing for better validation of near-surface model results. Such observations were not available in 2017 and 2018 (first thermistors at −1 m or lower), preventing us from validating model results closer to the surface in those years.

At both sites, modeled meltwater percolation (contoured by blue lines) did not reach the depth of the uppermost thermistor (gray lines) during the 2017 and 2018 melt seasons (Figs 3b, e). During summer 2019, modeled meltwater percolated much deeper than in the previous summers, reaching -1 m at EKT and -4 m at Site J. However, observations do not show the same thermal signal of percolating meltwater, typically characterized by the snowpack and firn becoming isothermal (0°C). This results in large temperature differences (Figs 3c, f), with modeled temperatures up to $+13.9°$and $+10.8°C$ warmer at EKT and Site J, respectively, during summer 2019.

4. Model sensitivity

In this section, we investigate possible causes for the considerable differences between model results and observations highlighted above. We explore model sensitivity to input forcing and model parameters. Furthermore, we include a parameterization that accounts for shortwave radiation penetration into the snow and evaluate the impact on model results.

Henceforth, the simulations presented above are referred to as *sim_ref*. Because the sensitivity experiments at Site J and EKT portray an almost identical picture, for brevity and clarity, only results from Site J are presented here and discussed in detail. Results from EKT are summarized in the Supplementary material (Figs S5–S8).

4.1. Model forcings

The meteorological observations used to force the model can be prone to errors. Here we test how such errors could affect model results by homogeneously perturbing the five meteorological input variables one by one, and re-running the model with the new input forcings (Fig. 4). Applied perturbations are guided by instrument accuracy as declared by the manufacturer (Table I). For example, we perturb air temperature by $\pm 1°C$ when the manufacturer stated accuracy is $0.6°C$, etc. Furthermore, for each of the input variables, we explore a scenario that, on average, comes close to relative surface height observations (shown in orange in Fig. 4).

These experiments suggest that the discrepancies between the reference simulation and observations cannot be explained by errors in input forcing or instrument accuracy. The perturbations required to match the measured surface height are extreme and far from being physically reasonable, e.g.$-5°C$ to air temperature, -50% to relative humidity, etc. Finally, given the large differences between model results and measurements, we are confident that not even the effect of combined perturbations (e.g. perturbing simultaneously two or more variables within reasonable limits) could explain the discrepancies.

Figure 4 indicates that, while positive perturbations typically produce more surface lowering, this is not the case for the wind speed. In fact, because turbulent fluxes at our sites are generally negative, higher wind speeds would cause more negative fluxes resulting in less surface lowering.
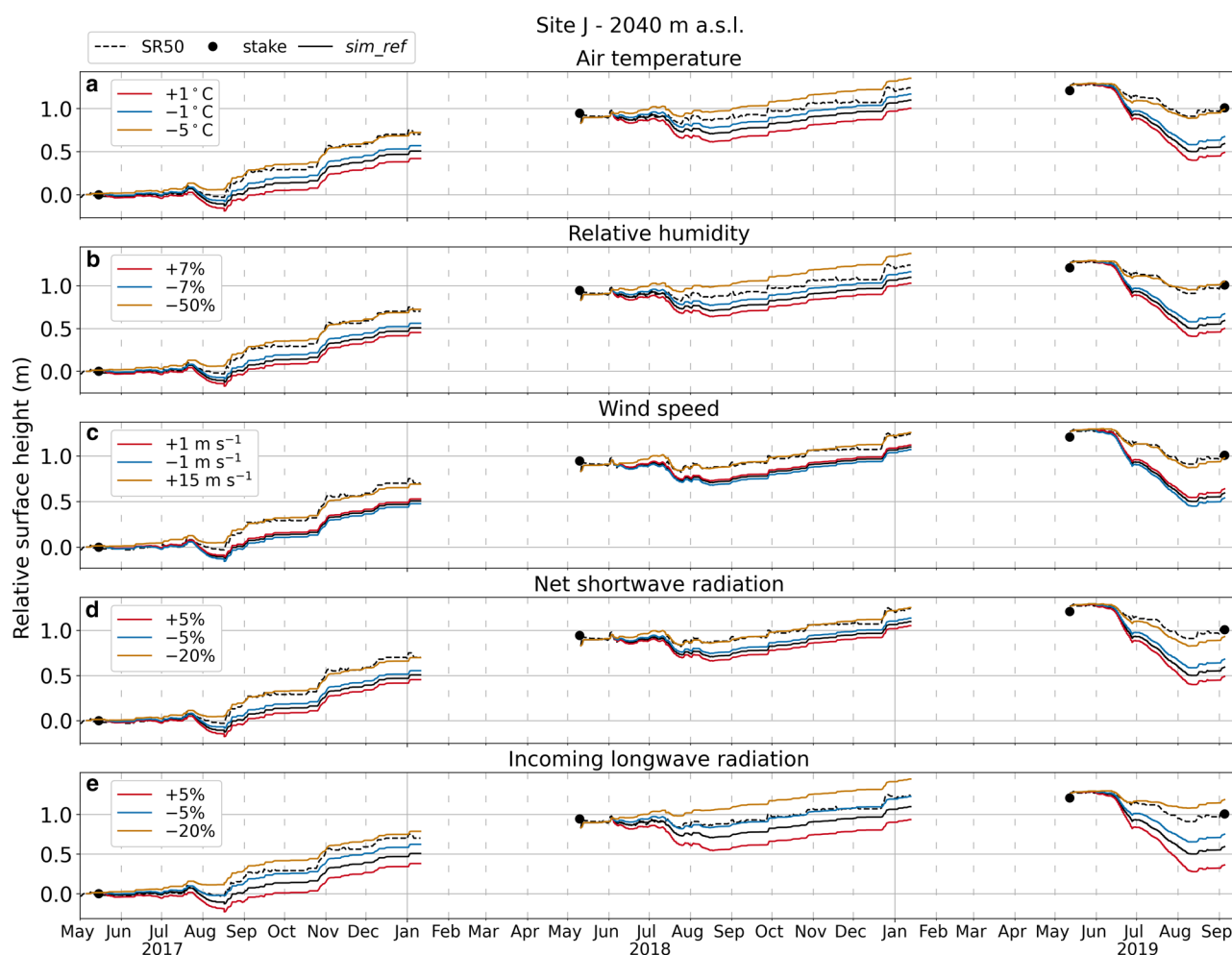

Fig. 4. Modeled hourly relative surface height compared to measurements from AWS sonic ranger (SR50) and ablation stake at Site J for simulations with different model forcings: (a) air temperature, (b) relative humidity, (c) wind speed, (d) net shortwave radiation and (e) incoming longwave radiation.

4.2. Model parameters and parameterizations

Model parameters and parameterizations (e.g. turbulent fluxes, thermal conductivity, etc.) used in the reference simulation are taken from the literature rather than calibrated to match the observations. To further investigate possible causes for the mismatch between model results and observations in *sim_ref*, here we test the model sensitivity to different choices of model parameters and parameterizations.

We perturb the surface roughness for momentum used in the reference simulation for the calculation of the turbulent heat fluxes ($z_{0m} = 0.1$ mm) by increasing and decreasing it by one order of magnitude (Fig. 5a). We change the new snow density from 350 kg m^{-3} to 300 and 400 kg m^{-3} (Fig. 5b). Thermal conductivity (κ) determines subsurface temperature evolution; thus, it controls the ground heat flux calculation, ultimately affecting the surface energy balance. Several different parameterizations for thermal conductivity exist in the literature. Here we replace the one used in the reference simulation (Douville and others, 1995) with four others following Reijmer and Hock (2008): Van Dusen and Washburn (1929); Sturm and others (1997); Östin and Andersson (1991); Jansson (1901) (Fig. 5c). Similarly, we replace the irreducible water content parameterization by Schneider and Jansson (2004) used in the reference simulation with the one presented in Coléou and Lesaffre (1998) (Fig. 5d). Finally, we turn off the densification parameterization (Fig. 5d).

As evident from Figure 5, the model is not sensitive to these perturbations and changes. Differences to *sim_ref* are barely detectable in most cases. Changes in surface roughness for momentum by an order of magnitude only slightly change the simulations. It should be noted that because the model uses the parameterization by Andreas (1987), surface roughness lengths for heat and moisture are computed as a function of z_{0m}; thus, they are also affected by these perturbations.

While not directly affecting the surface energy balance, the fresh snow density parameter controls the conversion of melt into surface height change. Higher densities cause less surface lowering and vice versa. This is only noticeable when significant accumulation occurred before or during the melt season, e.g. in 2017 and 2018 at Site J (Fig. 5b). Overall, simulation results are barely affected by the experiments. Thus, uncertainties in roughness lengths, snow density and thermal conductivity cannot explain the discrepancies between the reference simulation and observations.

4.3. Penetration of shortwave radiation

Although a well-documented physical process (e.g. Schlatter, 1972; Colbeck, 1989; Brandt and Warren, 1993), the penetration of shortwave radiation into the snowpack is not included in our model, consistently with most state of the art surface energy-balance models, including the most recent versions of RCMs such as MARv3.12, HIRHAM5 and RACMOv2.3p2 (Mankoff and others, 2021). Few studies have investigated the effect of shortwave radiation penetration on the surface energy balance in Greenland (Van Den Broeke, 2008; Kuipers Munneke and others, 2009) and in the Antarctic Peninsula (Kuipers Munneke and others, 2012). Here we use the same approach as Kuipers Munneke and others (2009), described in detail in the Appendix, to assess whether including this process in our model could explain the differences from the observations presented above.

The penetration of shortwave radiation, as described in this parameterization, strongly depends on the thickness of the fictitious surface layer, which is not to be confused with the thickness of the subsurface layers (see the Appendix for details and Kuipers Munneke and others (2009)). This calibration parameter controls
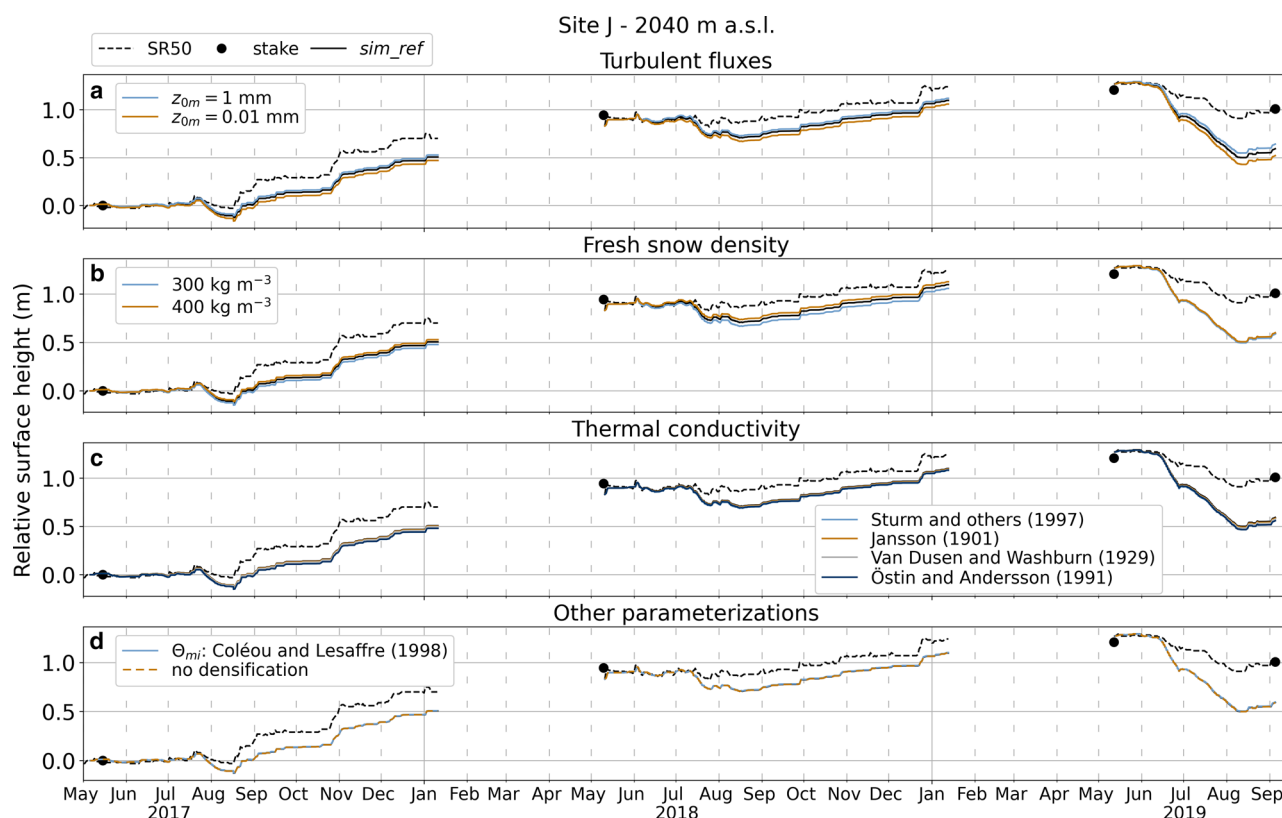

Fig. 5. Model sensitivity to choice of model parameters and parameterizations at Site J. Modeled hourly relative surface height compared to measurements from sonic ranger (SR50) and ablation stake for simulations with (a) perturbed roughness length for momentum and (b) perturbed fresh snow density, (c) different thermal conductivity and (d) densification and irreducible water content (Θ_{mi}) parameterizations.
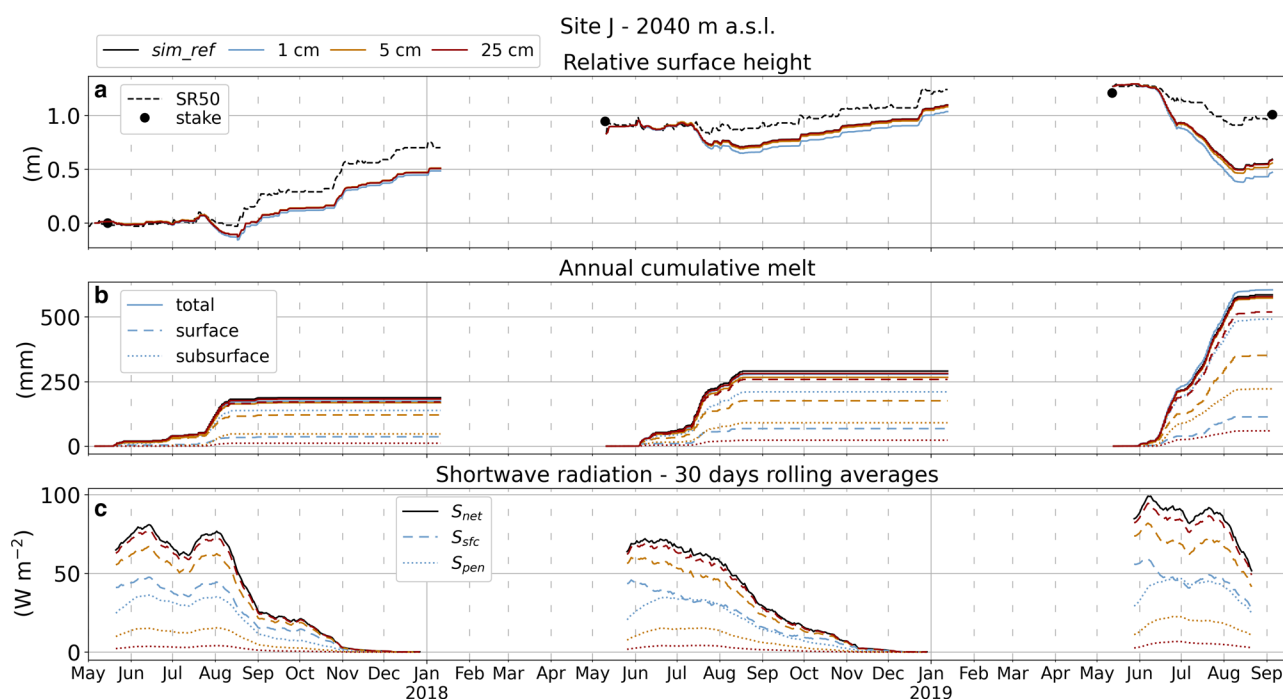
Fig. 6. (a) Hourly relative surface height, (b) annual cumulative total, surface and subsurface melt and (c) 30-day rolling average of shortwave radiation components (S_{net}, S_{sfc} and S_{pen}) for simulations including radiation penetration at Site J. Results using different fictitious surface layer thicknesses are presented: 1 cm in cyan, 5 cm in orange and 25 cm in red. Reference simulation in solid black and observations in dashed black. Reference simulation only has total cumulative melt and S_{net}.

the amount of net shortwave radiation (S_{net}) that penetrates into the subsurface (S_{pen}) and the amount that is absorbed by the surface (S_{sfc}), affecting the surface energy balance and the warming of the subsurface. Here we present simulations using three different fictitious surface layer thicknesses: 0.01, 0.05 and 0.25 m (Fig. 6). For small thicknesses, more shortwave radiation is allowed to penetrate into the subsurface while for thicker layers most of the shortwave radiation is absorbed by the surface: S_{pen}/S_{net} = 43, 17 and 4% on average for the 0.01, 0.05 and 0.25 m simulations respectively (Fig. 6c). If a very thick fictitious surface layer is considered all the net shortwave radiation would stay at the surface, replicating the assumptions made in the reference simulation when radiation penetration is not considered.

Both relative surface height and total melt vary very little from *sim_ref* (Figs 6a, b). This is because radiation penetration allows melting to happen also in the subsurface (e.g. firn temperature = 0°C). Hence, the thinner the fictitious surface layers, the greater the melt in the subsurface layers, thereby compensating for less melt at the surface (Fig. 6b).

More details on the effects of radiation penetration are highlighted when looking at surface and subsurface temperatures. Figure 7 shows hourly temperatures for a 2 weeks period at Site J during the 2019 melt season. During the first days, the near-surface snowpack is mostly temperate (i.e. at 0°C), indicating the presence of meltwater. Starting 28 June the air temperature drops resulting in a cooling of both the surface and the subsurface and an almost complete halt in melt. Surface temperature is higher for simulations with thicker fictitious surface layers, and it is the highest for the reference simulation (Fig. 7a), where radiation penetration is not considered. However, the simulated T_s is higher than the observations for all the simulations. In contrast, subsurface temperatures, at both 0.1 and 0.25 m depth, are warmer for simulations with a thinner fictitious surface layer when more energy penetrates into the subsurface. Despite subsurface temperatures being sensitive to the choice of the fictitious surface layer thickness necessary to model the penetration of solar radiation, the experiments indicate that the omission of

this process in the reference simulation cannot account for the differences between model results and observations.

4.4. Deep water percolation

Deep water percolation through preferential flow paths is a well-known process that affects water redistribution through the snow and firn matrix (e.g. Sturm and Holmgren, 1993; Humphrey and others, 2012; Cox and others, 2015). However, this process is often not included in the subsurface models used in surface energy-balance models, which employ a tipping bucket approach to simulate water percolation from one layer to the next one. This is also the case for RCMs such as MAR, HiRAM and RACMO2. Marchenko and others (2017) used a simple statistical approach to parameterize deep water percolation, showing that accounting for this process improves the simulations of subsurface temperature.

Here, we apply the same approach, described in detail in the Appendix, to assess whether parameterizing deep water percolation could improve our model results presented above. Surface meltwater is redistributed to deeper subsurface layers following a probability density function that solely depends on a prescribed depth of maximum percolation (e.g. depth below which no water is allocated). Following Marchenko and others (2017), we test three different probability density functions, uniform (UNI), linear (LIN) and normal law (NORM), and three different maximum percolation depths, 2.5, 5.0 and 7.5 m.

Accounting for deep water percolation reduces the *sim_ref* total melt at Site J over the entire study period between 1.4 and 9.7%, depending on the probability density function and the maximum percolation depth used (Table S1). Surface melt is reduced the most when more water is redistributed from the surface to deeper subsurface layers (Fig. 8b). This is the case for simulations with deeper maximum percolation depths (e.g. 7.5 m) and using functions that allocate more water at depth (e.g.UNI). However, despite the decrease in melt, the relative surface height lowers more in these simulations than in *sim_ref* (Fig. 8a). This is the result of redistributing meltwater and refreezing away from the
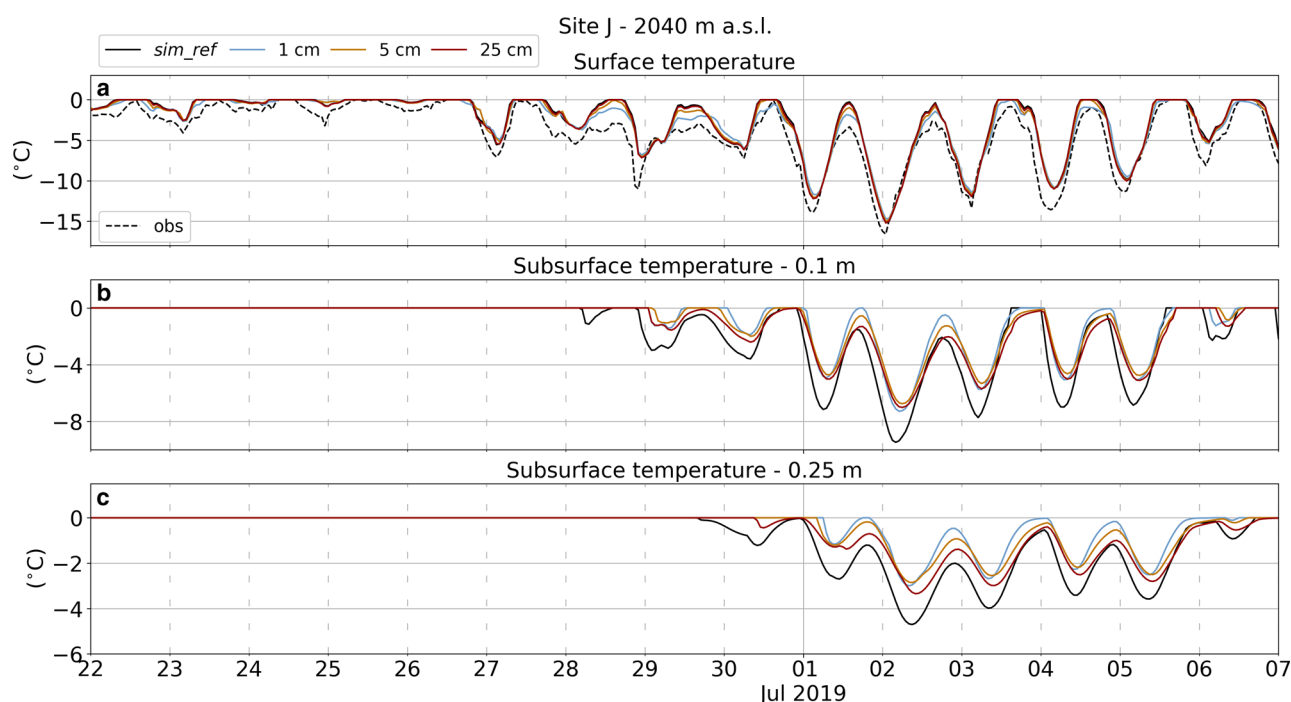
Fig. 7. Details of hourly surface temperature (a) and subsurface temperature at 0.10 m (b) and 0.25 m (c) depth for simulations including radiation penetration at Site J for a 2 weeks period between the end of June and the beginning of July 2019. Results using different fictitious surface layer thicknesses are presented: 1 cm in cyan, 5 cm in orange and 25 cm in red. Reference simulation in solid black and observations in dashed black.

surface. In a tipping bucket percolation model, in fact, the refreezing capacity of a layer is completely exhausted before water is allowed to percolate to the next layer. Thus, in *sim_ref* refreezing rapidly increases the density of the surface layer making the surface lowering less compared to simulations with deep percolation. On the contrary, when water is allowed to percolate at depth, refreezing happens at multiple layers delaying the appearance of liquid water in the subsurface (Fig. S1) and keeping the density of the surface layer low.

The redistribution of refreezing at depth that follows deep water percolation also affect the subsurface temperature. All simulations overestimate the subsurface temperature at depths where water is allowed to percolate, showing larger temperature differences between model and observations compared to *sim_ref* (Fig. S2). Temperature differences are the largest for simulations that redistribute more water at depth, which are the same that also reduce melt the most.

These experiments indicate that, although accounting for deep water percolation slightly decreases melt, it makes the comparison with observations even worse than for the reference simulation.

5. Forcing the model with observed surface temperature

Surface temperature is a crucial variable used to determine several surface energy fluxes (Eqn (1)). Non-linear feedbacks when closing the energy budget with the skin layer formulation may cause errors in the modeled surface temperature. Therefore, we force the model with surface temperatures derived from measurements of outgoing longwave radiation. This experiment aims to evaluate the behavior of the model when the surface temperature is constrained by observations rather than modeled internally and to explore potential sources of errors responsible for the differences
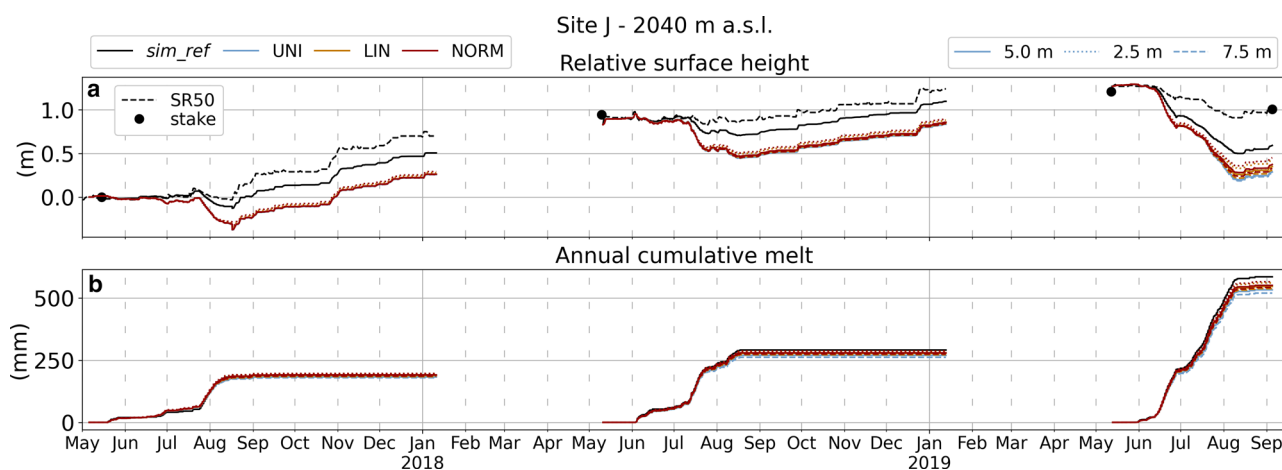

Fig. 8. (a) Hourly relative surface height and (b) annual cumulative melt for simulations including deep water percolation at Site J. Results using different percolation probability density functions (UNI in cyan, LIN in orange and NORM in red) and depth of maximum percolation (2.5 m dotted, 5.0 m solid and 7.5 m dashed) are presented. Reference simulation in solid black and observations in dashed black.
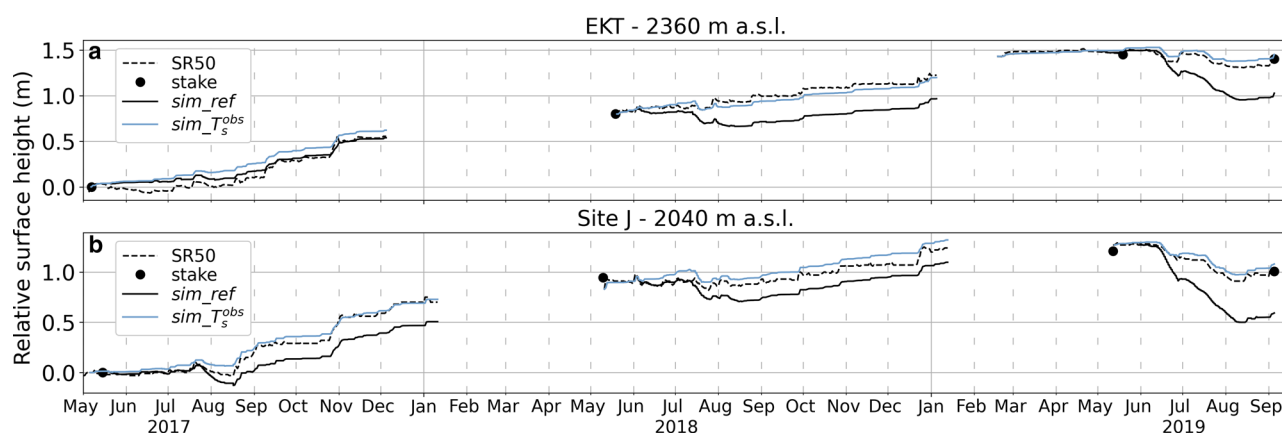
Fig. 9. Modeled hourly relative surface height compared to measurements from AWS sonic ranger (SR50) and ablation stake at (a) EKT and (b) Site J for simulations forced with observed surface temperature ($sim\_T_s^{obs}$) and reference simulations (sim_ref).

between model results and observations. Henceforth these simulations are referred to as $sim\_T_s^{obs}$.

Figure 9 shows that the simulated relative surface height matches well with the observations at both sites. Surface temperature observations cannot be used for validation since they are already used as input; however, we compare model results to subsurface firn temperature observations. In this experiment, modeled firn temperature (Fig. S3) compares better to thermistor string measurements than in sim_ref (Fig. 3). Maximum positive temperature differences are reduced from $+13.9°$C at EKT and $+10.8°$C at Site J for the reference simulations to $+6.54°$ and $+1.72°$C. Furthermore, the melt-water percolation signal (e.g. isothermal firn $0°$C) is better represented in this simulation. At EKT during the 2019 melt season, percolation never reached the depth of the first thermistor (gray line in Fig. S3b), consistent with observations. At Site J, during the 2019 melt season, simulated meltwater reached the depths of the first two thermistors consistent with the temperature observations (Fig. S3e). Total melt over the entire study period is 2.7 and 3.6 times smaller at Site J (397 vs 1064 mm) and EKT (217 vs 783 mm), respectively, for $sim\_T_s^{obs}$ compared to sim_ref.

Despite these results comparing well with observations, there are some underlying issues with these types of simulations. When the model is forced with observations of surface temperature all the fluxes in Eqn (1) are taken or computed from measurements. S_{in}, S_{ref}, L_{in} and L_{out} are directly taken from observations. H, LE and Q_R are computed as functions of observations. Q_G is computed from measured surface temperature, previous time step subsurface temperatures and parameterized thermal conductivity. This causes a problem in the surface energy-balance closure. In fact, when melt is not occurring (e.g. $T_s < 0$ and $Q_M = 0$), the sum of all the fluxes may be different from zero. In contrast, when there is melt, the sum of all fluxes is always zero because the melt energy is set to be equal to the sum of all the other fluxes. This may lead to a negative computed

Q_M, which further underlines the problem in closing the energy balance. However, only this happens six times at Site J and three times at EKT with values of $Q_M < 1$ W m^{-2}.

At both our sites, the imbalance (Fig. 10) is non-negligible, with averages of 10.7 and 6.1 W m^{-2} at EKT and Site J, respectively and daily means exceeding 50 W m^{-2} at times. Furthermore, the imbalance exhibits a clear seasonal signal at both sites. It is positive during the melt season and turns negative in winter, with greater magnitude during the summer (Fig. 10).

6. Discussion

Simulated surface height changes at our two study sites match well with the observations when the model is forced with surface temperature ($sim\_T_s^{obs}$) computed from observations of outgoing longwave radiation. However, when the skin layer formulation is used to close the surface energy balance (sim_ref), the model overestimates surface lowering and melt consistently during all three melt seasons. Sensitivity to both input forcings and model parameters has been extensively tested and cannot explain the differences between simulations and observations.

We also exclude insufficient accounting for firn compaction processes as possible cause for the discrepancy noting that our model includes a densification module although only considering dry firn. Also, our ablation stake and the SR50 both measure the thinning of the seasonal snow and firn layer between the base of the structure carrying the sensor and the surface, including both surface lowering due to melt and compaction. However, if compaction was underestimated the discrepancy between simulations and observations would be even larger. Furthermore, our conclusions are backed up by warmer surface and subsurface temperatures compared to observations.
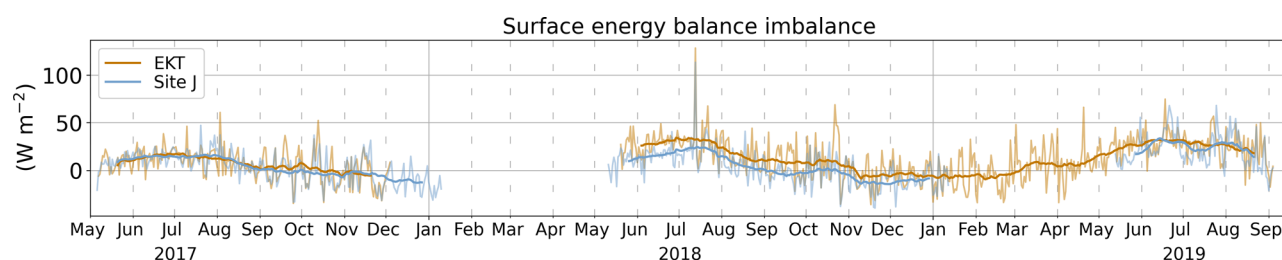

Fig. 10. Daily mean and 30-day rolling average of the imbalance in surface energy-balance calculations at EKT and Site J for simulations forced with observed surface temperature ($sim\_T_s^{obs}$).
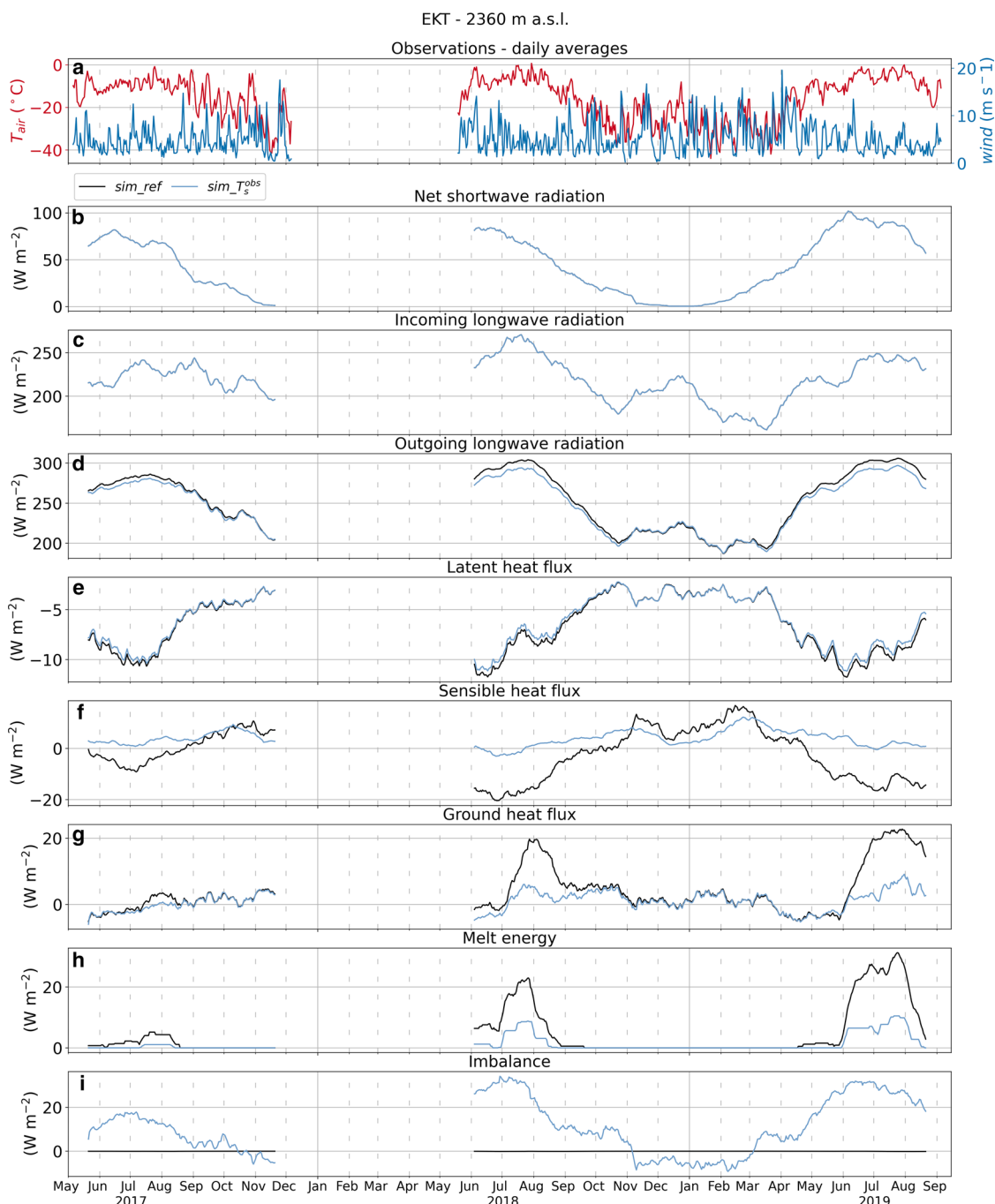
Fig. 11. Daily averages of air temperature and wind speed and 30-day rolling averages of surface energy-balance components for *sim_ref* and *sim_T_s^obs* simulations at EKT: (a) air temperature and wind speed, (b) net shortwave radiation, (c) incoming longwave radiation, (d) outgoing longwave radiation, (e) latent heat flux, (f) sensible heat flux, (g) ground heat flux, (h) energy available for melt and (i) surface energy-balance residual.

6.1. Surface energy fluxes

Figure 11 shows the 30-day rolling averages of the surface energy fluxes for both *sim_ref* and *sim_T_s^obs* at EKT (fluxes at Site J are shown in Fig. S4). S_{net} and L_{in} are identical for both simulations because they are taken from observations. L_{out} and LE show small differences while larger discrepancies are found in H, Q_G and Q_M.

Differences are generally small in winter but pronounced during the melt season. H in *sim_ref* is considerably more negative in the summer than H in *sim_T_s^obs*, which is mostly positive and small in magnitude (Fig. 11f). In contrast, Q_G in *sim_ref* is considerably more positive during the melting season compared to *sim_T_s^obs* (Fig. 11g). The few other studies modeling the surface energy balance at weather station locations in the percolation area of southwest Greenland (Charalampidis and others, 2015;

Vandecrux and others, 2017, 2018; Samimi and others, 2021) depict a similar picture to the one presented here, although simulated years are different. For example, Vandecrux and others (2018) used the skin layer formulation and found that, on average, H was negative during summer. In contrast, Samimi and others (2021) forced their model with observations of surface temperature and H was generally positive during summer.

6.2. Surface temperature

H and Q_G strongly depend on surface temperature. H depends on the gradient between the air and the surface temperatures, while Q_G depends on the gradient between the surface and the subsurface temperatures. Observations at our sites show that during the
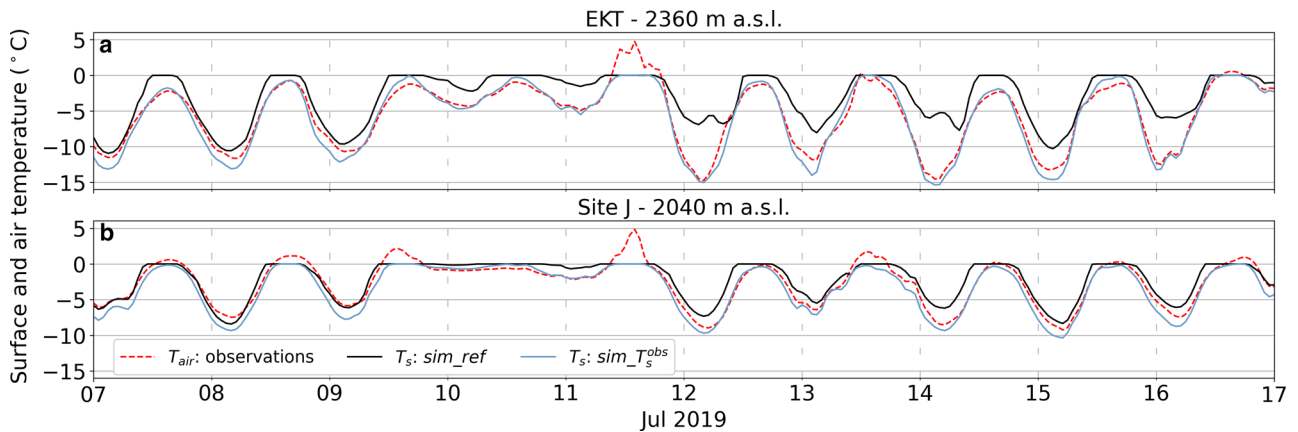
Fig. 12. Hourly air temperature from observations and surface temperature for the *sim_ref* and *sim_T*$_s^{obs}$ simulations at EKT and Site J for the period between 7 and 17 July 2019. The surface temperature for the *sim_T*$_s^{obs}$ simulation is retrieved from observations of outgoing longwave radiation.

melt season surface conditions are characterized by a strong diurnal cycle (Fig. 12). The surface melts during the second half of the day and refreezes at night. Thus, the balance between the temperature of the air, the surface and the subsurface is delicate. Slightly different modeled surface temperatures can cause both H and Q_G to change sign from negative to positive and vice versa, drastically changing the surface energy balance and modeled melt.

Figure 12 shows that the observed surface temperature used to force the *sim_T*$_s^{obs}$ simulation is lower than the modeled one in the *sim_ref* simulation. Every time the air temperature (red line) falls between the observed (*sim_T*$_s^{obs}$) and modeled (*sim_ref*) surface temperature, the H will differ in sign between the two different simulations, adding or subtracting energy available for the surface melt. The effect on the surface energy balance, however, is counterintuitive; in fact, the *sim_ref* simulation, which overestimates melt, is the one exhibiting a negative H during the summer, which results in cooling of the surface (Fig. 11f). The 30-day rolling average of Q_G is positive for both simulations but much larger for *sim_ref*, resulting in more energy directed toward the surface, allowing for more warming and more melting (Fig. 11g).

The effect of a slightly different modeled surface temperature is less pronounced for L_{out} and LE. L_{out} directly depends on the surface temperature but not on its gradient with either the air or the subsurface; thus, it is not affected by the strong diurnal cycle described above. On the other hand, LE depends on the gradient between the air and the surface temperature, but its effect is filtered by the computation of the vapor pressure of the air and the surface.

Because these processes are non-linear, it is difficult to attribute the differences in melt between the two simulations to a particular flux. For example, Q_G is highly sensitive to warming of the subsurface through latent heat released by refreezing meltwater. This means that the larger Q_G in the *sim_ref* simulation may be a consequence of more melting and not the cause.

6.3. Closing the energy balance

Although the *sim_T*$_s^{obs}$ simulation captures surface lowering and melt during the summer well, results are inconsistent since the energy balance is not closed. The problem of surface energy-balance closure and residuals (Fig. 10) has been known for decades in the fields of boundary layer meteorology (e.g. Mauder and others, 2020). The imbalance has been attributed to neglected processes and uncertainties, typically assumed to be negligible for a horizontally uniform 2-D exchange surface without a canopy, with

fluxes perpendicular to the surface. Although we are not aware of any mention in glaciological studies, Wang and others (2021) address this problem on seasonally frozen ground. They found that accounting for soil ice heat storage and latent heat of soil ice phase improved the estimates of the ground heat flux, reducing the imbalance. Our model currently treats the liquid water content in the subsurface separately from the dry part of the firn, perhaps accounting for liquid water heat storage would lead to a better representation of Q_G.

Direct observations of the turbulent fluxes, e.g. using the eddy-covariance technique (Smeets and Broeke, 2008b), and the ground heat flux are recommended by the boundary layer meteorology community to reduce the imbalance when investigating the energy-balance closure problem (Mauder and others, 2020). Unfortunately, such observations are rare in the percolation zone of the Greenland ice sheet. Furthermore, another process that is not included in our model and may affect the surface energy-balance calculations and closure is windpumping. Strong winds can disrupt the thermal regime of near-surface snow (Colbeck, 1989) affecting Q_G. However, the sustained wind speeds required for this to happen are large ($>10\,\mathrm{m\,s^{-1}}$) and seldom recorded during the summer when the energy-balance residual is the largest (Figs 11a, i). Ultimately a better understanding of these problems will help improve our models, including when the skin layer formulation is used.

7. Conclusions

We applied an energy-balance model forced by weather station observations at two sites (2040 and 2360 m a.s.l.) in the percolation zone of the ice sheet over 3 years. Simulated melt and subsurface firn temperatures in summer were overestimated by the model compared to observations. The mismatch could not be explained by uncertainties in input forcings nor by choice of model parameters or various model parameterizations.

While the causes for the mismatch between simulations using the skin-layer formulation and observations remain elusive and need further investigation, our results highlight the complexity of energy-balance modeling in the percolation zone of the Greenland ice sheet. At these elevations, surface conditions during the summer are characterized by a strong diurnal cycle, with air temperatures barely above freezing. The surface melts and refreezes during melt days, and subsurface temperatures are modulated by the release of latent heat from refreezing water.

The mismatch is also of concern since RCMs, such as MAR, RACMO and HIRHAM, have used the same skin layer

formulation to close the surface energy balance and compute the mass balance of the entire ice sheet (Christensen and others, 2006; Fettweis and others, 2017; Noël and others, 2018) and resulting contributions to sea level. Although RCMs being more complex than our model, e.g. they rely on parameterization also for the net shortwave radiation and incoming longwave radiation, our results suggest that melt estimates relying on the skin layer formulation may be biased and should be carefully evaluated and validated.

When our model was forced by observed surface temperatures, simulated surface height changes matched observations well; however, the energy balance is no longer closed, leaving unexplained residuals. The two different types of simulations, using the skin layer formulation and forcing the model with observed surface temperatures, yielded pronounced differences for the sensible and the ground heat flux, which both are directly dependent on the surface temperature. Due to pronounced diurnal cycles in surface temperature during the melt season, accurately modeling the surface temperature is crucial for reliable melt estimates in this region.

Better observations and measurements are needed to better understand the physical processes and mechanisms driving the surface energy balance in this area of the ice sheet. In particular, high-resolution temperature and moisture measurements of the near-surface seasonal snow would help to better constrain the role of the ground heat flux and the water content in the energy budget.

Processes such as the formation of impermeable ice layers are making the percolation zone increasingly more important in the mass budget of the Greenland ice sheet and a potential contributor to sea level rise. It is thus fundamental to further investigate the problems presented here to improve melt estimates of both point energy-balance models and the RCMs.

References

Andreas EL (1987) A theory for the scalar roughness and the scalar transfer coefficients over snow and sea ice. *Boundary-Layer Meteorology* **38**(1), 159–184. doi: 10.1007/BF00121562

Beljaars ACM and Holtslag AAM (1991) Flux parameterization over land surfaces for atmospheric models. *Journal of Applied Meteorology* **30**(3), 327–341. doi: 10.1175/1520-0450(1991)030<0327:FPOLSF>2.0.CO;2

Braithwaite RJ and Olesen OB (1990) A simple energy-balance model to calculate ice ablation at the margin of the Greenland ice sheet. *Journal of Glaciology* **36**(123), 222–228. doi: 10.1017/S0022143000009473

Brandt RE and Warren SG (1993) Solar-heating rates and temperature profiles in Antarctic snow and ice. *Journal of Glaciology* **39**(131), 99–110. doi: 10.3189/s0022143000015756

Brun E, Martin E, Simon V, Gendre C and Coleou C (1989) An energy and mass model of snow cover suitable for operational avalanche forecasting. *Journal of Glaciology* **35**(121), 333–342. doi: 10.1017/S0022143000009254

Cazenave A, and 89 others (2018) Global sea-level budget 1993–present. *Earth System Science Data* **10**, 1551–1590. doi: 10.5194/essd-10-1551-2018

Charalampidis C and 9 others (2015) Changing surface-atmosphere energy exchange and refreezing capacity of the lower accumulation area, West Greenland. *The Cryosphere* **9**(6), 2163–2181. doi: 10.5194/tc-9-2163-2015

Christensen OB and 6 others (2006) The HIRHAM Regional Climate Model, Version 5. Technical report.

Colbeck SC (1989) Snow-crystal growth with varying surface temperatures and radiation penetration. *Journal of Glaciology* **35**(119), 23–29. doi: 10.3189/002214389793701536

Coléou C and Lesaffre B (1998) Irreducible water saturation in snow: experimental results in a cold laboratory. *Annals of Glaciology* **26**, 64–68. doi:10.3189/1998AoG26-1-64-68

Cox C, Humphrey N and Harper J (2015) Quantifying meltwater refreezing along a transect of sites on the Greenland icesheet. *The Cryosphere* **9**, 691–701. doi: 10.5194/tcd-8-5485-2014

Douville H, Royer JF and Mahfouf JF (1995) A new snow parameterization for the Météo-France climate model: part I: validation in stand-alone experiments. *Climate Dynamics* **12**(1), 21–35. doi: 10.1007/BF00208760

Enderlin EM and 5 others (2014) An improved mass budget for the Greenland ice sheet. *Geophysical Research Letters* **41**(3), 866–872. doi: 10.1002/2013GL059010

Fausto RS and 11 others (2018) A Snow Density Dataset for Improving Surface Boundary Conditions in Greenland Ice Sheet Firn Modeling.

Fettweis X, Tedesco M, van den Broeke M, and Ettema J (2011) Melting trends over the Greenland ice sheet (1958–2009) from spaceborne microwave data and regional climate models. *The Cryosphere* **5**(2), 359–375. doi: 10.5194/tc-5-359-2011

Fettweis X (2017) Reconstructions of the 1900–2015 Greenland ice sheet surface mass balance using the regional climate MAR model. *The Cryosphere* **11**(2), 1015–1033. doi: 10.5194/tc-11-1015-2017

Flanner MG and Zender CS (2006) Linking snowpack microphysics and albedo evolution. *Journal of Geophysical Research Atmospheres* **111**(12), 1–12. doi: 10.1029/2005JD006834

Greuell W and Konzelmann T (1994) Numerical modelling of the energy balance and the englacial temperature of the Greenland ice sheet. Calculations for the ETH-Camp location (West Greenland, 1155 m a.s.l.). *Global and Planetary Change* **9**(1–2), 91–114. doi: 10.1016/0921-8181(94)90010-8

Henneken EA, Bink NJ, Vugts HF, Cannemeijer F and Meesters AG (1994) A case study of the daily energy balance near the equilibrium line on the Greenland ice sheet. *Global and Planetary Change* **9**(1–2), 69–78. doi: 10.1016/0921-8181(94)90008-6

Herron MM and Langway CC (1980) Firn densification: an empirical model. *Journal of Glaciology* **25**(93), 373–385. doi: 10.3189/S0022143000015239

Hock R and Holmgren B (2005) A distributed surface energy-balance model for complex topography and its applications to Storglaciaren. *Journal of Glaciology* **51**(172), 25–36. doi: 10.3189/172756505781829566

Huai B, van den Broeke MR and Reijmer CH (2020) Long-term surface energy balance of the western Greenland ice sheet and the role of large-scale circulation variability. *The Cryosphere* **14**(11), 4181–4199. doi: 10.5194/tc-14-4181-2020

Humphrey NF, Harper JT and Pfeffer WT (2012) Thermal tracking of meltwater retention in Greenland's accumulation area. *Journal of Geophysical Research* **117**, 02083. doi: 10.1029/2011JF002083

Intergovernmental Panel on Climate Change (2014) Observations: Cryosphere. In Intergovernmental Panel on Climate Change (ed.), *Climate Change 2013–The Physical Science Basis: Working Group I Contribution to the Fifth Assessment Report of the Intergovernmental Panel on Climate Change*, 317–382, Cambridge University Press, Cambridge. doi: 10.1017/CBO9781107415324.012.

Jansson M (1901) Über die Wärmeleitungsfähigkeit des Schnees. *Öfversigt af Kongl. Vétenskaps-Akad. Förhandlinger* **58**, 207–222. doi: 10.1051/jphystap:019020010012101

Kameda T and 5 others (1995) Melt features in ice cores from Site J, southern Greenland: some implications for summer climate since AD 1550. *Annals of Glaciology* **21**, 51–58. doi: 10.1017/S0260305500015597

Kuipers Munneke P and 6 others (2009) The role of radiation penetration in the energy budget of the snowpack at Summit, Greenland. *The Cryosphere* **3** (2), 155–165. doi: 10.5194/tc-3-155-2009

Kuipers Munneke P and 5 others (2011) A new albedo parameterization for use in climate models over the Antarctic ice sheet. *Journal of Geophysical Research Atmospheres* **116**(5), 1–10. doi: 10.1029/2010JD015113

Kuipers Munneke P, van den Broeke MR, King JC, Gray T and Reijmer CH (2012) Near-surface climate and surface energy budget of Larsen C Ice Shelf, Antarctic Peninsula. *The Cryosphere* **6**(2), 353–363. doi: 10.5194/tc-6-353-2012

Kuipers Munneke P and 5 others (2018) The K-transect on the western Greenland ice sheet: surface energy balance (2003–2016). *Arctic, Antarctic, and Alpine Research* **50**(1), 1–13. doi: 10.1080/15230430.2017.1420952

Li J and Zwally HJ (2004) Modeling the density variation in the shallow firn layer. *Annals of Glaciology* **38**, 309–313. doi: 10.3189/172756404781814988

MacFerrin MJ (2018) *Rapid expansion of Greenland's low-permeability ice slabs in a warming climate.* Ph.D. thesis, University of Colorado.

MacFerrin MJ and 13 others (2019) Rapid expansion of Greenland's low-permeability ice slabs. *Nature* **573**, 403–407. doi: 10.1038/s41586-019-1550-3

MacFerrin MJ, Stevens CM, Vandecrux B, Waddington ED and Abdalati W (2022) The Greenland firn compaction verification and reconnaissance (FirnCover) dataset, 2013–2019. *Earth System Science Data* **14**(2), 955–971. doi: 10.5194/essd-14-955-2022

Machguth H and 9 others (2016) Greenland meltwater storage in firn limited by near-surface ice formation. *Nature Climate Change* **6**(4), 390–393. doi: 10.1038/nclimate2899

Mankoff KD and 15 others (2021) Greenland ice sheet mass balance from 1840 through next week. *Earth System Science Data* **13**(10), 5001–5025. doi: 10.5194/essd-13-5001-2021

Marchenko S and 6 others (2017) Parameterizing deep water percolation improves subsurface temperature simulations by a multilayer firn model. *Frontiers in Earth Science* **5**, 00016. doi: 10.3389/feart.2017.00016

Mauder M, Foken T and Cuxart J (2020) Surface-energy-balance closure over land: a review. *Boundary-Layer Meteorology* **177**(2–3), 395–426. doi: 10.1007/s10546-020-00529-6

Morlighem M and 31 others (2017) BedMachine v3: complete bed topography and ocean bathymetry mapping of Greenland from multibeam echo sounding combined with mass conservation. *Geophysical Research Letters* **44**(21), 051–11. doi: 10.1002/2017GL074954

Mote TL (2007) Greenland surface melt trends 1973–2007: evidence of a large increase in 2007. *Geophysical Research Letters* **34**(22). doi: 10.1029/2007GL031976.

Mouginot J and others (2019) Forty-six years of Greenland ice sheet mass balance from 1972 to 2018. *Proceedings of the National Academy of Sciences of the United States of America* **116**(19), 9239–9244. doi: 10.1073/pnas.1904242116

Munro DS (1990) Comparison of melt energy computations and ablatometer measurements on melting ice and snow. *Arctic and Alpine Research* **22**(2), 153–162. doi: 10.1080/00040851.1990.12002777

Noël B and 6 others (2016) A daily, 1 km resolution data set of downscaled Greenland ice sheet surface mass balance (1958–2015). *The Cryosphere* **10**(5), 2361–2377. doi: 10.5194/tc-10-2361-2016

Noël B and 1 others (2018) Modelling the climate and surface mass balance of polar ice sheets using RACMO2 – part 1: Greenland (1958–2016). *The Cryosphere* **12**(3), 811–831. doi: 10.5194/tc-12-811-2018

Noël B, van de Berg WJ, Lhermitte S, and van den Broeke MR (2019) Rapid ablation zone expansion amplifies north Greenland mass loss. *Science Advances* **5**(9), 2–11. doi: 10.1126/sciadv.aaw0123

Östin R and Andersson S (1991) Frost growth parameters in a forced air stream. *International Journal of Heat and Mass Transfer* **34**(4–5), 1009–1017. doi: 10.1016/0017-9310(91)90012-4

Panofsky HA and Dutton JA (1984) *Atmospheric Turbulence: Models and Methods for Engineering Applications.* John Wiley & Sons, New York.

Pavlis NK, Holmes SA, Kenyon SC and Factor JK (2012) The development and evaluation of the Earth Gravitational Model 2008 (EGM2008). *Journal of Geophysical Research: Solid Earth* **117**(4), 1–38. doi: 10.1029/2011JB008916

Porter C and 28 others (2018) ArcticDEM. doi: 10.7910/DVN/OHHUKH.

Reijmer CH and Hock R (2008) Internal accumulation on Storglaciären, Sweden, in a multi-layer snow model coupled to a distributed energy- and mass-balance model. *Journal of Glaciology* **54**(184), 61–72. doi: 10.3189/002214308784409161

Rennermalm ÅK and 12 others (2021) Shallow firn cores 1989–2019 in southwest Greenland's percolation zone reveal decreasing density and ice layer thickness after 2012. *Journal of Glaciology* **68**, 1–12. doi: 10.1017/jog.2021.102

Samimi S, Marshall SJ, Vandecrux B and MacFerrin M (2021) Time-domain reflectometry measurements and modeling of firn meltwater infiltration at DYE-2, Greenland. *Journal of Geophysical Research: Earth Surface* **126**(10), 006295. doi: 10.1029/2021jf006295.

Schlatter TW (1972) The local surface energy balance and subsurface temperature regime in Antarctica. *Journal of Applied Meteorology* **11**(7), 1048–1062. doi: 10.1175/1520-0450(1972)011<1048:TLSEBA>2.0.CO;2

Schneider T and Jansson P (2004) Internal accumulation in firn and its significance for the mass balance of Storglaciären, Sweden. *Journal of Glaciology* **50**(168), 25–34. doi: 10.3189/172756504781830277

Shepherd A and 86 others (2020) Mass balance of the Greenland ice sheet from 1992 to 2018. *Nature* **579**(7798), 233–239. doi: 10.1038/s41586-019-1855-2

Smeets CJ and Broeke MR (2008a) Temporal and spatial variations of the aerodynamic roughness length in the ablation zone of the Greenland ice sheet. *Boundary-Layer Meteorology* **128**(3), 315–338. doi: 10.1007/s10546-008-9291-0

Smeets CJ and Broeke MR (2008b) The parameterisation of scalar transfer over rough ice. *Boundary-Layer Meteorology* **128**(3), 339–355. doi: 10.1007/s10546-008-9292-z

Smeets PC and 7 others (2018) The K-transect in west Greenland: automatic weather station data (1993–2016). *Arctic, Antarctic, and Alpine Research* **50**(1). doi: 10.1080/15230430.2017.1420954.

Sturm M and Holmgren J (1993) Rain-induced water percolation in snow as detected using heat flux transducers. *Water Resources Research* **29**(7), 2323–2334. doi: 10.1029/93WR00609

Sturm M, Holmgren J, König M and Morris K (1997) The thermal conductivity of seasonal snow. *Journal of Glaciology* **43**(143), 26–41. doi: 10.1017/S0022143000002781

Tedesco M (2007) Snowmelt detection over the Greenland ice sheet from SSM/I brightness temperature daily variations. *Geophysical Research Letters* **34**(2), 1–6. doi: 10.1029/2006GL028466

Van As D and 5 others (2012) Large surface meltwater discharge from the Kangerlussuaq sector of the Greenland ice sheet during the record-warm year 2010 explained by detailed energy balance observations. *The Cryosphere* **6**(1), 199–209. doi: 10.5194/tc-6-199-2012

Van Den Broeke M (2008) Partitioning of melt energy and meltwater fluxes in the ablation zone of the west Greenland ice sheet. *The Cryosphere* **2**(2), 179–189. doi: 10.5194/tc-2-179-2008

Van Den Broeke MR, Smeets CJP, and Van De Wal RS (2011) The seasonal cycle and interannual variability of surface energy balance and melt in the ablation zone of the west Greenland ice sheet. *The Cryosphere* **5**(2), 377–390. doi: 10.5194/tc-5-377-2011

Van Dusen MS and Washburn EW (1929) Thermal Conductivity of Non-metallic solids. In *International Critical Tables of Numerical Data, Physics, Chemistry and Technology*, volume 5, 216–217, McGraw-Hill, New York.

Vandecrux B, Fausto RS, Langen PL, van As D and Macferrin M (2018) Drivers of Firn Density on the Greenland Ice Sheet Revealed by Weather Station Observations and Modeling. doi: 10.1029/2017JF004597.

Vandecrux B and 12 others (2020a) Firn cold content evolution at nine sites on the Greenland ice sheet between 1998 and 2017. *Journal of Glaciology* **66** (258), 591–602. doi: 10.1017/jog.2020.30

Vandecrux B and 22 others (2020b) The firn meltwater Retention Model Intercomparison Project (RetMIP): evaluation of nine firn models at four weather station sites on the Greenland ice sheet. *The Cryosphere* **14**(11), 3785–3810. doi: 10.5194/tc-14-3785-2020

Wang J and 6 others (2021) Improving ground heat flux estimation: considering the effect of freeze/thaw process on the seasonally frozen ground. *Journal of Geophysical Research: Atmospheres* **126**(24), 1–23. doi: 10.1029/2021jd035445

Warren SG (1984) Optical constants of ice from the ultraviolet to the microwave. *Applied Optics* **23**(8), 1206–1225. doi: 10.1364/AO.23.001206

Warren SG, Brandt RE and Grenfell TC (2006) Visible and near-ultraviolet absorption spectrum of ice from transmission of solar radiation into snow. *Applied Optics* **45**(21), 5320–5334. doi: 10.1364/AO.45.005320

Appendix A. Penetration of shortwave radiation

We compute the penetration shortwave radiation following the approach by Kuipers Munneke and others (2009), which is based on the method described by Brandt and Warren (1993) and applied by Van Den Broeke (2008). The parameterization employs the two stream approach from Schlatter (1972) to calculate the attenuation of shortwave radiation in the firn at different wavelengths.

First, the observed incoming shortwave radiation is divided into spectral bands using reference solar spectra from Brandt and Warren (1993) and Kuipers Munneke and others (2009). In total 118 wavelength bands from 299 to 2999 nm are used. Next the amount of shortwave radiation $S_{\text{pen}}(z)$ that penetrates to a depth z is given by the following equation from Schlatter (1972):

$$S_{\text{pen}}(z) = \int_{\lambda} S_{\text{in}}^{\lambda}(1 - m_{\lambda})e^{-k_{\lambda}z} \mathrm{d}\lambda, \tag{A.1}$$

where λ is the wavelength, S_{in}^{λ} is the incoming shortwave radiation at given wavelength λ, m_{λ} is the multi-spectral albedo and k_{λ} is the multi-spectral extinction coefficient. Multi-spectral albedo and extinction coefficient are calculated following the approach of Brandt and Warren (1993), using effective firn grain size, firn density and Mie scattering coefficients from Warren (1984), updated with values from Warren and others (2006). Finally, the total shortwave radiation S_{pen} that penetrates into the subsurface is calculated as $S_{\text{pen}} = \sum^{\text{layers}} S_{\text{pen}}(z)$, and $S_{\text{pen}}(z)$ is added to the respective subsurface layer. The surface energy-balance equation (Eqn (1)) becomes the following:

$$S_{\text{sfc}} + L_{\text{in}} + L_{\text{out}} + H + LE + Q_{\text{R}} + Q_{\text{G}} + Q_{\text{M}} = 0, \tag{A.2}$$

$$S_{\text{sfc}} = S_{\text{net}} + S_{\text{pen}} = S_{\text{in}} + S_{\text{ref}} + S_{\text{pen}}, \tag{A.3}$$

where S_{sfc} is the shortwave radiation absorbed by the surface, S_{net} is the net shortwave radiation, S_{pen} is the shortwave radiation that penetrates into the subsurface and the other variables are the same as in Eqn (1). Fluxes toward the surface are defined as positive.

For an infinitesimal surface layer, as it is the case for the skin layer formulation used in our model, all the net shortwave radiation would penetrate into the subsurface. To control the amount of S_{net} that penetrates into the subsurface (S_{pen}) and that is absorbed by the surface (S_{sfc}), previous studies (Van Den Broeke, 2008; Kuipers Munneke and others, 2009) have attributed a fictitious thickness to the surface. This affects only the radiation penetration parameterization and is not to be confused with the layer thickness in the subsurface model. This fictitious surface thickness represents an important calibration parameter and sensitivity to it is discussed in detail in the 'Results' Section.

The evolution of the effective firn grain size required to compute multi-spectral albedo and extinction coefficients is modeled following the approach presented in Kuipers Munneke and others (2011). This method accounts for dry snow metamorphism, wet snow metamorphism, refreezing of liquid water and fresh snow. The effect of dry snow metamorphism is calculated using parametric curves from Flanner and Zender (2006), while wet snow metamorphism is described by the parameterization presented in Brun and others (1989). The grain size of refrozen water is set to 1.5 mm following Kuipers Munneke and others (2011) while the grain size of fresh snow is set to 0.1 mm based on snow pit observations at out study sites.

Appendix B. Deep water percolation

Following Marchenko and others (2017) preferential water flow to deeper layers in the snowpack and firn is simulated by redistributing surface meltwater among subsurface layers before refreezing is calculated. The amount of water allocated to each subsurface layer is determined by a probability density function $\text{PDF}(z, z_{\text{lim}})$, where z is the layer depth and z_{lim} is the user defined depth of maximum percolation. Three different PDFs are tested in Marchenko and others (2017) and included in this study as well.

PDF_{uni} describes uniform water infiltration. Water is redistributed equally to each subsurface layer between the surface and z_{lim}:

$$\text{PDF}_{\text{uni}}(z, z_{\text{lim}}) = \begin{cases} \frac{1}{z_{\text{lim}}}, & \text{if } z \leq z_{\text{lim}} \\ 0, & \text{otherwise} \end{cases} \tag{B.1}$$

PDF_{lin} describes linear water infiltration. Redistributed water linearly decreases with depth at a constant rate reaching 0 at z_{lim}:

$$\text{PDF}_{\text{lin}}(z, z_{\text{lim}}) = \begin{cases} \frac{2(z_{\text{lim}} - z)}{z_{\text{lim}}^2}, & \text{if } z \leq z_{\text{lim}} \\ 0, & \text{otherwise} \end{cases} \tag{B.2}$$

PDF_{norm} describes water infiltration following the normal law. Water is redistributed following the normal probability density function with SD $\sigma = z_{\text{lim}}/3$, implying that 99.7% of the water is allocated above z_{lim}:

$$\text{PDF}_{\text{norm}}(z, z_{\text{lim}}) = 2\frac{\exp\left(-(z^2/2\sigma^2)\right)}{\sigma\sqrt{2\pi}} \tag{B.3}$$